Offline Parameter Self-Learning Method for General-Purpose PMSM Drives with Estimation Error Compensation

Qiwei Wang, Guoqiang Zhang, *Member, IEEE*, Gaolin Wang, *Senior Member, IEEE*, Chengrui Li, and Dianguo Xu, *Fellow, IEEE*

***Abstract*—Offline parameter identification of permanent magnet synchronous machines (PMSMs) is of great importance for general-purpose drives with sensorless control. This paper proposes an amplitude-auto-adjusting signal injection (ASI) method for the parameter self-learning of PMSMs at standstill considering inverter nonlinearities and the digital time-delay effect. The ASI method achieves the inductance identification process under various *dq*-axis currents and at the same time prevents the unexpected rotor rotation during the self-commissioning process. For the test PMSM, the spatial inductance maps of *dq*-axes and *abc*-phases concerning the magnetic saturation and cross-coupling effects are identified along with the stator resistance. To enhance the estimation accuracy, an error model of the inverter nonlinearities in *dq*-axes is established, and a compensation method independent of inverter parameters is proposed based on the Hermite interpolation. In addition, the influence of the digital time-delay effect is analyzed and compensated based on the transient model of the circuits. The effectiveness of the proposed parameter self-learning scheme is confirmed on a 2.2-kW PMSM drive. The accuracy of the experimental results is validated by finite element analysis (FEA) on the test machine.**

***Index Terms*—Permanent magnet synchronous machine, offline parameter self-learning, magnetic saturation, cross-coupling, inverter nonlinearity, digital time-delay effect.**

I. INTRODUCTION

PERMANENT magnet synchronous machines (PMSMs) have been drawing increasing attention because of high efficiency, high power factor and good dynamic performance, etc. [1]-[8]. More and more advanced control schemes have been applied to further improve the operation performance of PMSMs, which usually require machine parameters [9]-[15]. Thus the parameters should be identified before motor startup, otherwise the drive system would not perform well. Moreover, because some machine control schemes strongly rely on accurate parameters such as the stator resistance and the *dq*-axis inductances, etc., the offline parameter identification is supposed to provide more parameter information to support various control strategies [8]. Meanwhile, for enhancing the availability of control system, greater demands were placed on the generality of parameter self-learning method [10], [14]. Hence, parameter self-learning method should be applicable for drive systems with different types of inverters and machines.

Signal injection method is an effective way in parameter identification. As for the stator resistance identification, a linear increasing current is injected into the *d*-axis, and the estimated resistance can be calculated by the linear regression for the gradient calculation according to the multipoint information of currents and voltages [8], [12]. The inductance identification of PMSMs can be generally classified into two different approaches. The first approach estimates inductances by the amplitude and the frequency of injected high frequency (HF) signals [6], [10], [12]. In [12], the inductance identification was achieved with HF sinusoidal signal injection. At the same time, a supplementary positive DC signal was injected into the *d*-axis to prevent the rotation of rotor. In [10], the phase angle between the voltage and current vectors was applied to attenuate the inductance identification error. The injected signals consist of both AC and DC signals, where the DC signal sets the operating point and the AC signal estimates the inductance at that point. The second approach focuses on the flux linkage identification, from which the inductances can be then derived [13]-[15]. The aforementioned methods have rendered the parameter self-learning a great improvement. However, better solutions for enhancing the accuracy of the parameter identification still need to be investigated. Furthermore, the prevention of the rotor rotation during the parameter identification process requires investigation.

Inverter nonlinearities consist of several factors, where the dead time effect and the parasitic capacitance effect are the major contributors to the carrier voltage distortion. The parasitic capacitance effect induces terminal voltage error mainly at lower current level, whereas the dead time effect is the dominant error at higher current level [19], [20]. The sign function of phase currents was used to compensate the error of inverter nonlinearities in [1], [11]. In [12], [21], the inverter parameter equation was applied to describe the error of inverter nonlinearities in order to realize the compensation. However, the inverter nonlinearities are too complex to be fully compensated only by sign function, and the inverter parameter

Manuscript received November 27 2018; revised December 19 2018; accepted February 13, 2019. This work was supported by the Research Fund for the National Science Foundation of China under Grant (51877054, 51807037 and 51690182), and the Power Electronics Science and Education Development Program of Delta Group (DREM2018001). (*Corresponding author: Guoqiang Zhang*.)

The authors are with the School of Electrical Engineering and Automation, Harbin Institute of Technology, Harbin 150001, China (e-mail: wqw0543 @163.com; ZhGQ@hit.edu.cn; WGL818@hit.edu.cn; chengruili1994@ yahoo.com; xudiang@hit.edu.cn).

This article has been accepted for publication in a future issue of this journal, but has not been fully edited. Content may change prior to final publication. Citation information: DOI 10.1109/TPEL.2019.2900559, IEEE Transactions on Power Electronics

equation is sensitive to the inverter parameters. In order to improve the generality of the self-commissioning method, better error compensation methods require further research. Besides inverter nonlinearities, there is an inevitable execution time delay in digital control system of machine drive [22]-[24]. The time-delay effect will be obvious when the frequency of the injected HF signal is high enough. The error due to the digital time-delay effect in offline parameter identification has not been studied yet.

The ASI method is proposed in this paper for estimating the parameters characteristics of PMSMs at standstill considering inverter nonlinearities and the digital time delay. Firstly, the mathematical algorithm for calculating the *dq*-axis and *abc*-phase inductances is proposed by analyzing the influence of the magnetic saturation and cross-coupling effects on inductance. The mathematical expression of *dq*-axis and *abc*-phase inductances considering the mutual inductance are presented, and the relationship between the cross-coupling effect and the *q*-axis armature reflection is revealed. Secondly, by analyzing the motion equation of PMSMs and the RL equivalent circuit model of stator windings, the derivation process of the ASI method is proposed to keep the machine standstill during the parameter identification by adjusting the amplitude of the injected signals automatically for both *dq*-axes. Then, the error model of inverter nonlinearities is established to analyze its effects on *dq*-axis inductance identification, and then a corresponding compensation method independent of the parameters of inverters is proposed based on the Hermite interpolation, which realizes the voltage error compensation in full current range and is independent of inverter parameters. Meanwhile, the estimation error caused by the digital time delay is analyzed and corrected with the transient model of the circuits, which has not been studied yet. Finally, the *dq*-axis spatial flux linkage maps and the *dq*-axis spatial inductance maps can be obtained, and then the *abc*-phase inductances can also be calculated with the given algorithm which play an important role in some control schemes and fault diagnosis methods of PMSMs [16]-[18].

This paper proceeds as follows: Section II analyzes the influence of the magnetic saturation and cross-coupling effects on *dq*-axis and *abc*-phase inductances in different operating conditions. Section III introduces the proposed ASI method. Section IV investigates the error characteristics of inverter nonlinearities and the digital time delay and proposes the compensation method. Experimental results of parameters and the FEA validation are in Section V.

II. Analysis of the Inductances of PMSMs in Different Operating Conditions

The influence of magnetic saturation and cross-coupling on *dq*-axis inductances is investigated in this section. Meanwhile, the existence of the mutual inductance between *dq*-axes is proved. A calculation algorithm of *abc*-phase inductances considering magnetic saturation and cross-coupling is given. The whole process of the self-commissioning scheme is introduced.

A. Analysis of dq-Axis Inductances and abc-Phase Inductances under Magnetic Saturation and Cross-Coupling

As for PMSMs, the varying flux linkages in magnetic paths of the stator and rotor change the magnetic flux density B and result in the variation of permeability μ of yokes, which indicates the magnetic saturation. According to the definition equation of inductance, the inductance of manganic path can be represented as

$$L = N^2 \cdot \lambda = N^2 \frac{\mu A}{l} \tag{1}$$

where N is the number of stator winding turns, λ is the magnetic conductance, A and l represent the average sectional area and the length of manganic path respectively.

The operating conditions of PMSMs include rated condition, overload condition with high level *q*-axis current i_q and flux-weakening condition with minus *d*-axis current i_d. Different operating conditions result in different degree of magnetic saturation and cross-coupling, then affect the inductance.

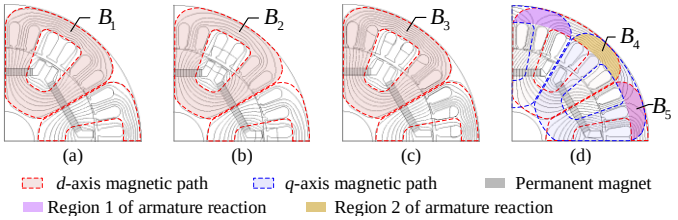

Fig. 1. Simulation results of magnetic saturation in different operating conditions. (a) i_d=0, i_q=0. (b) i_d=-i_n, i_q=0. (c) i_d=i_n, i_q=0. (d) i_d=0, i_q=i_n.

Fig. 1 shows the magnetic saturation effect of the test PMSM under different operating conditions by FEA, where i_n is the per unit value of current, B_l is the magnetic flux density whose degree can be indicated by the density of magnetic lines, l=1, 2⋯5. As shown in Fig. 1(a)-(c), the increase of the *d*-axis current will aggravate the magnetic saturation. The *d*-axis magnetic flux density distribution satisfies $B_3>B_1>B_2$, and then the *d*-axis inductance satisfies $L_2>L_1>L_3$. In Fig. 1(a) and (d), the existence of i_q causes the *q*-axis armature reaction, which aggravates and weakens the magnetic flux density in region 1 and in region 2, respectively. Considering the magnetic saturation, the overall magnetic flux density decrease, $B_4>B_1>B_5$.

In addition, the *q*-axis armature reaction influences inductances by redistributing the magnetic field of yokes, resulting in the cross-coupling and the mutual inductance between *dq*-axes. The simulation results of the test PMSM are shown in Fig. 2.

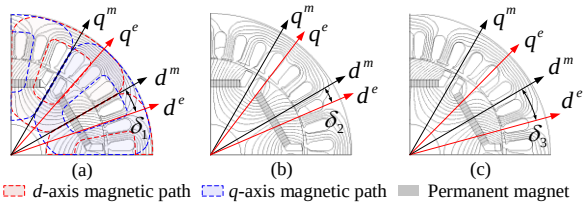

Fig. 2. Simulation results of cross-coupling in different operating conditions. (a) i_d=0, i_q=i_n. (b) i_d=0, i_q=0.5i_n. (c) i_d=-i_n, i_q=i_n.

The *q*-axis armature reactance causes a bias angle δ between the composite magnetic field and the permanent magnetic field. d^e and q^e represent the *dq*-axes of the composite magnetic field, respectively. d^m and q^m are the *dq*-axes of the permanent magnetic field, respectively. With the *q*-axis armature reactance, the cross-coupling occurs between d^m- and q^m-axes. The magnitude of δ is positively related to the degree of the *q*-axis armature reaction. Increasing the *q*-axis current and giving the *d*-axis demagnetization current will aggravate the *q*-axis armature reaction and increase the angle, $\delta_3>\delta_1>\delta_2$, as shown in Fig. 2.

Considering the cross-coupling, the reference frames of PMSMs are illustrated in Fig. 3, where the blue line represents the *dq*-axes of the permanent magnetic field, and the red line represents the *dq*-axes of the composite magnetic field.

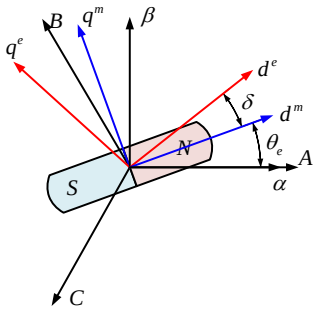

Fig. 3. Relations among the reference frames.

The *abc*-phase inductances can be presented as (2), where L_{aa}, L_{bb} and L_{cc} are the *abc*-phase self-inductances. M_{ab}, M_{bc}, M_{ca}, M_{ba}, M_{cb} and M_{ac} are the mutual incremental inductances of *abc*-phases. L_{sn} and M_{sn} are the magnitudes of *n*th order of self- and mutual inductances in the stationary reference frame, *n*=1, 2, 3 …. Remaining the DC and the second-order harmonic inductances, *dq*-axis inductances are obtained by transforming (2) into the rotary *dq* reference frame,

$$\begin{cases} L_{dd} = L_{s0} + M_{s0} + \left(L_{s2}/2 + M_{s2}\right)\cos 2\delta \\ L_{qq} = L_{s0} + M_{s0} - \left(L_{s2}/2 + M_{s2}\right)\cos 2\delta \\ L_{dq} = L_{qd} = \left(L_{s2}/2 + M_{s2}\right)\sin 2\delta \end{cases} \tag{3}$$

where L_{dd} and L_{qq} are the self-inductances of *dq*-axes. L_{dq} and L_{qd} are the mutual inductances between *dq*-axes which are not zero. According to the characteristics of PMSMs, the relation of the magnitudes of the DC and the second-order harmonic inductances can be expressed as

$$M_{s2} = L_{s2},\ M_{s0} \approx 0.5L_{s0}\,. \tag{4}$$

By substituting (4) into (3), the results can be obtained,

$$\begin{cases} \delta = \operatorname{atan}(2L_{dq}/(L_{dd} - L_{qq}))/2 \\ M_{s0} = (L_{dd} + L_{qq})/6 \\ M_{s2} = (L_{dd} - L_{qq})/3\cos 2\delta \end{cases}. \tag{5}$$

If L_{dd}, L_{qq} and L_{dq} are obtained by inductance identification method, L_{s0}, L_{s2}, M_{s0} and M_{s2} are easily obtained by (5), and then the *abc*-phase inductances can be solved by (2).

In summary, the magnetic saturation effect affects the magnetic circuit inductance by influencing the degree of saturation of magnetic path, while the cross-coupling caused by the *q*-axis armature reaction results in mutual inductances between *dq*-axes. Besides the parameter identification, the mathematical analysis of mutual inductance based on the *q*-axis armature reaction has potential practical significance in improving the control performance and the accuracy of sensorless control.

B. Process and Principle of the Offline Parameter Identification

The signal injection method is applied in the self-commissioning process by using space vector pulse width modulation (SVPWM). During the whole process, the stator resistance is firstly estimated and then the *dq*-axis flux linkages. The *dq*-axis inductances are calculated by *dq*-axis flux linkages. Finally, the *abc*-phase inductances are obtained by (2)-(4).

The block diagram of the self-commissioning process is shown in Fig. 4. In the figure, u_{dr} and u_{qr} are the *dq*-axis voltages respectively, which can be regarded as a function of time. The stator resistance identification can be achieved by injecting a DC current with the gradually increasing amplitude into the *d*-axis and no signal injection in *q*-axis. During the resistance identification process, and the linear regression is used to enhance the robustness against undesired perturbations during the identification. The process of the resistance identification is introduced in the Section IV. A.

After that, the *dq*-axis flux linkage is identified with a hysteresis control based HF voltage injection method, which will be discussed in detail in Section III. As shown in Fig 4, u_{di} and u_{qi} are the injected square-wave voltages of the *d*- and *q*-axis respectively, and I_{xset} is the current setting of the hysteresis control based HF voltage injection method, which controls the voltage switching when absolute value the current is larger than I_{xset}, x= *d*, *q*. The injected voltage signal can be written as follows,

$$u_{xref}(k) = \begin{cases} U_{xout}, & \text{if } i_x(k) < -I_{xset} \\ -U_{xout}, & \text{if } i_x(k) > I_{xset} \\ u_{xref}(k-1), & \text{otherwise} \end{cases} \quad x = d, q\,. \tag{6}$$

$$\begin{cases} L_{aa} = L_{s0} + L_{s2}\cos 2(\theta_e + \delta) + \sum L_{sn}\cos 2n(\theta_e + \delta) \\ L_{bb} = L_{s0} + L_{s2}\cos 2(\theta_e + \delta - 2\pi/3) + \sum L_{sn}\cos 2n(\theta_e + \delta - 2\pi/3) \\ L_{cc} = L_{s0} + L_{s2}\cos 2(\theta_e + \delta + 2\pi/3) + \sum L_{sn}\cos 2n(\theta_e + \delta + 2\pi/3) \\ M_{ab} = M_{ba} = -M_{s0} - M_{s2}\cos 2(\theta_e + \delta + \pi/6) - \sum M_{sn}\cos 2n(\theta_e + \delta + \pi/6) \\ M_{bc} = M_{cb} = -M_{s0} - M_{s2}\cos 2(\theta_e + \delta - \pi/2) - \sum M_{sn}\cos 2n(\theta_e + \delta - \pi/2) \\ M_{ca} = M_{ac} = -M_{s0} - M_{s2}\cos 2(\theta_e + \delta + 5\pi/6) - \sum M_{sn}\cos 2n(\theta_e + \delta + 5\pi/6) \end{cases} \tag{2}$$

This article has been accepted for publication in a future issue of this journal, but has not been fully edited. Content may change prior to final publication. Citation information: DOI 10.1109/TPEL.2019.2900559, IEEE Transactions on Power Electronics

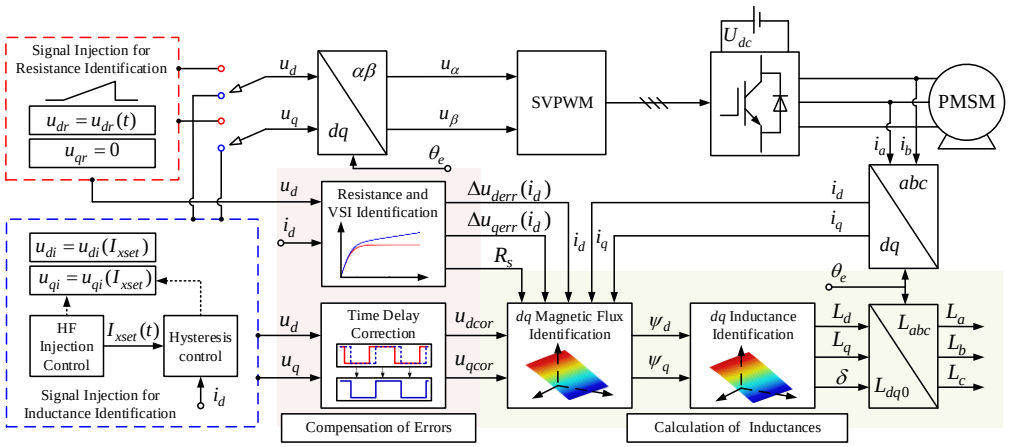

Fig. 4. Block diagram of the proposed offline parameter self-learning process.

The solving equation of the flux linkage can be expressed as

$$\psi_x = \int \left(u_{xref} - R_s i_x\right) \mathrm{d}t \quad x = d, q \tag{7}$$

where u_{xref} is the reference value of the injected voltage signal. U_{xout} is the amplitude of injected voltage, I_{xset} is the value of current setting which controls the magnitude of injection current as shown in (6).

Knowing the *dq*-axis flux linkages, inductances are then solved by differential operation of flux linkage to current. Most published papers about inductance identification neglected the mutual inductance between *dq*-axes, while, some papers did mention the mutual inductance but have not researched the solution principle thoroughly [10], [13]. The relation between *dq*-axis flux linkages and inductances is demonstrated as follows. The voltage equations at standstill is given as

$$\begin{bmatrix} u_d \\ u_q \end{bmatrix} = R_s \begin{bmatrix} i_d \\ i_q \end{bmatrix} + \begin{bmatrix} L_{dd} & L_{dq} \\ L_{qd} & L_{qq} \end{bmatrix} \frac{\mathrm{d}}{\mathrm{d}t} \begin{bmatrix} i_d \\ i_q \end{bmatrix} = R_s \begin{bmatrix} i_d \\ i_q \end{bmatrix} + \frac{\mathrm{d}}{\mathrm{d}t} \begin{bmatrix} \psi_d + \psi_f \\ \psi_q \end{bmatrix} \tag{8}$$

where ψ_f is permanent magnet flux linkage. The flux linkage can be expressed as the total differential of i_d and i_q, which can be presented as

$$\begin{cases} \mathrm{d}(\psi_d + \psi_f) = \mathrm{d}\psi_d = L_{dd}\mathrm{d}i_d + L_{dq}\mathrm{d}i_q \\ \mathrm{d}\psi_q = L_{qd}\mathrm{d}i_d + L_{qq}\mathrm{d}i_q \end{cases}. \tag{9}$$

ψ_d (i_d, i_q) and ψ_q (i_d, i_q) can be regarded as a function of i_d and i_q, and it is continuous and partial differentiable for any (i_d, i_q). Hence, the total differential equation (9) can be modified to the partial derivative equation shown as

$$\begin{bmatrix} \mathrm{d}\psi_d \\ \mathrm{d}\psi_q \end{bmatrix} = \begin{bmatrix} \dfrac{\mathrm{d}\psi_d}{\mathrm{d}i_d} & \dfrac{\mathrm{d}\psi_d}{\mathrm{d}i_q} \\ \dfrac{\mathrm{d}\psi_q}{\mathrm{d}i_d} & \dfrac{\mathrm{d}\psi_q}{\mathrm{d}i_q} \end{bmatrix} \begin{bmatrix} \mathrm{d}i_d \\ \mathrm{d}i_q \end{bmatrix} = \begin{bmatrix} L_{dd} & L_{dq} \\ L_{qd} & L_{qq} \end{bmatrix} \begin{bmatrix} \mathrm{d}i_d \\ \mathrm{d}i_q \end{bmatrix}. \tag{10}$$

L_{dd}, L_{dq}, L_{qd} and L_{qq} can be obtained by (10), and then the *abc*-phase inductances can be calculated by (2).

III. Proposed Hysteresis Control Based ASI Method for the Inductance Identification

In the self-commissioning process, the signal injected in the *d*-axis tends to align the rotor to the real *d*-axis, but the *q*-axis current produces electromagnetic torque, which may rotate the rotor and then affect the identified results. According to the dynamic characteristics of PMSMs, the proposed ASI method gives a control strategy for adjusting the amplitude of the injected *dq*-axes voltage signals automatically during the inductance self-learning process, so that the accuracy and the stability of the parameter identification can be improved.

First of all, the injected signal should not exceed the allowable range of voltage and current, which are represented by U_{lim} and I_{lim}, respectively. Assumptions are made before analysis: (1) The *dq*-axis circuits are described by the RL circuit model; (2) The machine inertia including the inertia of the connected mechanical load is constant; (3) The rotation angle of the rotor is small enough to neglect its influence on the estimated results. The instantaneous torque of the machine during the inductance identification process can be obtained from the torque equation, which is given as

$$T_{em} = p\left[\psi_f i_q + \left(L_d - L_q\right) i_d i_q\right] \tag{11}$$

where p is the number of pole-pairs. Since the injected voltages are the parameters directly controlled in the inductance identification as presented in (6), it is necessary to clarify the relation among the injection voltages, the feedback current and the rotation angle. Furthermore, because only the *q*-axis current produces torque, the movement state of PMSMs is investigated under a certain current setting I_{qset}. The movement of PMSMs is illustrated by the machine model shown in Fig. 5.

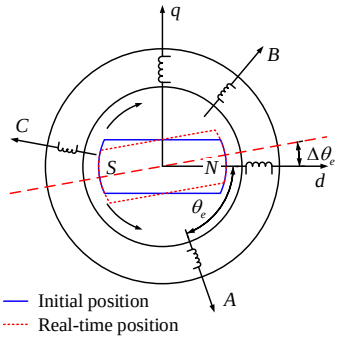

Fig. 5. Movement state of the PMSM during the inductance identification.

In Fig. 5, $\Delta\theta_e$ is the rotation angle of the rotor with the *q*-axis current varying from 0 to I_{qset} in the hysteresis control based ASI method. J is the inertia of the machine, and T_{em} is the electromagnetic torque. The motion equation of PMSMs is defined as

$$T_{em} = J\frac{\mathrm{d}^2\Delta\theta_e}{\mathrm{d}t^2} \tag{12}$$

where

$$\Delta\theta_e = \iint \frac{T_{em}}{J}\mathrm{d}t\mathrm{d}t\,. \tag{13}$$

The square-wave voltage with amplitude of U_q is injected into q-axis, and the q-axis induced current is expressed as

$$i_q = \frac{U_q}{R_s}\left(1-e^{-tR/Lq}\right). \tag{14}$$

Similarly, the d-axis induced current can be expressed as

$$i_d = \frac{U_d}{R_s}\left(1-e^{-tR/Ld}\right). \tag{15}$$

Equation (16) expresses the duration t_{set} with q-axis current varying from 0 to I_{qset}

$$t_{set} = -\frac{L_q}{R_s}\ln\left(1-\frac{I_{qset}R}{U_q}\right). \tag{16}$$

Since the injected signal is periodic, the rotation angle of the rotor and the electromagnetic torque are also periodic. Thus, it would be enough to analyze the machine rotation in a half injection period. According to (12)-(16), the relation between the rotation angle $\Delta\theta_e$ and the injected voltage U_d and U_q can be obtained for a certain I_{qset}. In this case, U_d is expressed as a function of U_q, I_{qset} and $\Delta\theta_e$, which can be shown as (17).

The q-axis current setting I_{qset} is the maximum value of the q-axis current. By the theory of RL circuit, the minimum value of the q-axis voltage can be written as

$$U_{qmin} = R_s I_{qset}\,. \tag{18}$$

The maximum value of the d-axis voltage can be written as

$$U_{dmax} = \sqrt{U_{lim}{}^2 - U_{qmin}{}^2}\,. \tag{19}$$

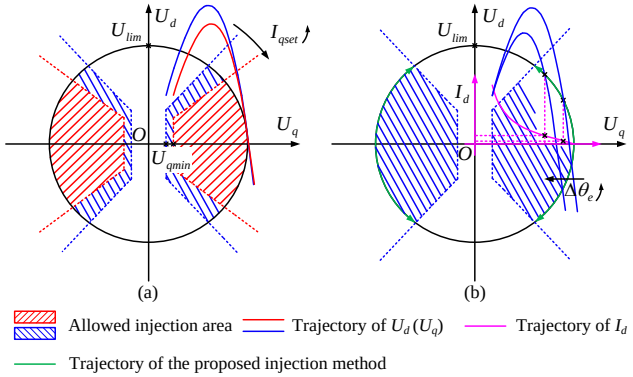

Fig. 6. Relations among U_d, U_q, I_{qset} and $\Delta\theta_e$. (a) Allowed injection area of U_d and U_q with different I_{qset}. (b) Voltage vector trajectory of the proposed injection method for a certain I_{qset}.

Fig. 6 illustrates the relations among U_d, U_q, I_{qset} and $\Delta\theta_e$. The shadow area is the allowed injection area of dq-axis voltage defined by (18) and (19). Fig. 6(a) shows that the greater the I_{qset} is, the smaller the allowed injection area will be. The trajectory of the proposed injection method in Fig. 6(b) indicates that the minimum rotor angle can be guaranteed when the U_d and U_q are located in the voltage limit circle. By changing the combination of dq-axis voltage, the inductance identification can be realized under any possible combinations of i_d and i_q.

Considering the actual operating condition of PMSMs, the inductances are identified in the range of $i_d \leqslant 0$ and $i_q > 0$. In order to avoid numerical discontinuities of the estimated dq-axis flux linkage, the no-torque condition when i_q is 0, should be considered [6]. Under the premise that I_{qset} is equal to 0, a hysteresis control with d-axis current setting I_{dset} is used to fulfill the inductance self-learning under no-torque condition. Based on the analysis in Section III, the proposed ASI method can determine the proper amplitude of U_d and U_q for different I_{dset} and I_{qset}, which achieves the inductance identification process under different dq-axis currents combinations and at the same time prevents the unexpected rotor rotation during the self-commissioning process. The selection rule for U_d, U_q, I_{dset} and I_{qset} of ASI method is described in Fig. 7. After the selection of voltages and currents, the injection method is realized by hysteresis control shown in (6).

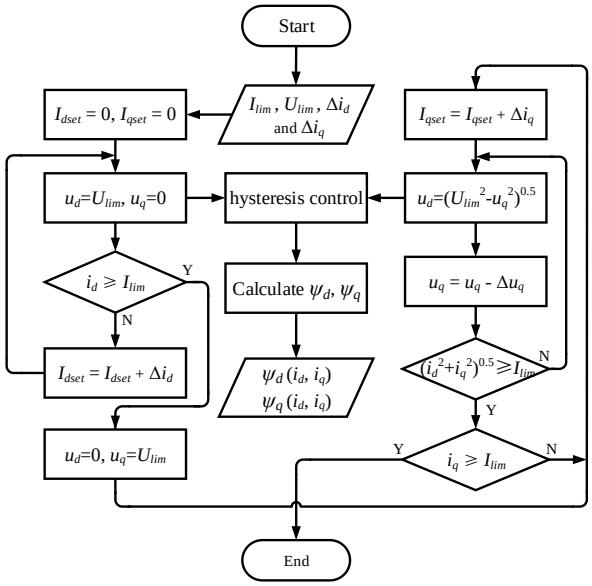

Fig. 7. Flowchart for the ASI method and the control method for the inductance self-learning under no-torque condition.

IV. Error Analysis of the Parameter Identification and the Compensation Method

A. Error Analysis of Inverter Nonlinearities and the Compensation Method

Both the dead time effect and the parasitic capacitance effect are major contributors to the carrier voltage distortion. Therefore, the inverter nonlinearities are too complex to be fully compensated only by the inverter parameter equation or sign function. Besides, inverter parameter equation relies on the parameters of inverters that are usually unknown to users. In this section, a general-purpose error compensation algorithm is proposed to identify and compensate the inverter nonlinearities regardless of inverter types. This method can be implemented simultaneously with the parameter self-learning process without additional operation.

According to [12], the *abc*-phase voltage and current under inverter nonlinearities can be expressed as

This article has been accepted for publication in a future issue of this journal, but has not been fully edited. Content may change prior to final publication. Citation information: DOI 10.1109/TPEL.2019.2900559, IEEE Transactions on Power Electronics

$$\begin{cases} U_d = \left(\Delta\theta_e - \dfrac{p\psi_f U_q}{R_s J} C_1\right) \dfrac{JR_s^2}{p\left(L_d - L_q\right)U_q C_2} \\ C_1 = \dfrac{1}{2}\left(\dfrac{L_q}{R_s}\ln\left(1-\dfrac{I_{qset}R_s}{U_q}\right)\right)^2 + \left(\dfrac{L_q}{R_s}\right)^2 \ln\left(1-\dfrac{I_{qset}R_s}{U_q}\right) + \left(\dfrac{L_q}{R_s}\right)^2 - \left(\dfrac{L_q}{R_s}\right)^2\left(1-\dfrac{I_{qset}R_s}{U_q}\right) \\ C_2 = \dfrac{1}{2}\left(\dfrac{L_q}{R_s}\ln\left(1-\dfrac{I_{qset}R_s}{U_q}\right)\right)^2 - \left(\dfrac{L_d}{R_s}\right)^2\left(1-\dfrac{I_{qset}R_s}{U_q}\right)^{L_q/L_d} - \left(\dfrac{L_q}{R_s}\right)^2\left(1-\dfrac{I_{qset}R_s}{U_q}\right) - \left(\dfrac{L_d L_q}{R_s L_d + R_s L_q}\right)^2\left(1-\dfrac{I_{qset}R_s}{U_q}\right)^{1+L_q/L_d} \\ \quad + \left(\dfrac{L_d L_q}{R_s L_d + R_s L_q} - \dfrac{L_d}{R_s} - \dfrac{L_q}{R_s}\right)\left(-\dfrac{L_q}{R_s}\ln\left(1-\dfrac{I_{qset}R_s}{U_q}\right)\right) + \left(-\left(\dfrac{L_d L_q}{R_s L_d + R_s L_q}\right)^2 + \left(\dfrac{L_q}{R_s}\right)^2 + \left(\dfrac{L_q}{R_s}\right)^2\right) \end{cases} \tag{17}$$

$$\begin{cases} u_x(i_x) = R_s i_x + u_{xerr}(i_x) \\ R_{xerr} = \dfrac{\mathrm{d}u_{xerr}}{\mathrm{d}i_x} \qquad x = a,b,c \\ R_x = R_s + R_{xerr} \end{cases} \tag{20}$$

where u_x is the phase voltage, u_{xerr} is the phase voltage error, R_x is the phase resistance and R_{xerr} is the nonlinear equivalent resistance. When phase current exceeds a certain value, the voltage error value u_{xerr} is a large constant and R_{xerr} is approximately equal to 0 [15], [20]. According to (20), the phase resistance R_x can be regarded as R_s at high current level. The *dq*-axis resistances have the same property [12], which can be proved by the coordinate transformation between *abc*-phases and *dq*-axes. This theory can be used for the resistance identification. The solving equation of the flux linkage can be changed to

$$\psi_x = \int (u_{xref} - u_{xerr}(i_x) - R_s i_x)\,\mathrm{d}t \qquad x = d,q\,. \tag{21}$$

A linear increasing current is injected into the *d*-axis for stator resistance identification. The resistance can be calculated by using the linear regression. The *d*-axis voltage of the stator resistance identification is shown in Fig. 8. In Fig. 8, u_d is the *d*-axis voltage and u_{derr} is the *d*-axis voltage error. R_{dn} is the gradient of the voltage line obtained by linear regression, n=0, 1…5.

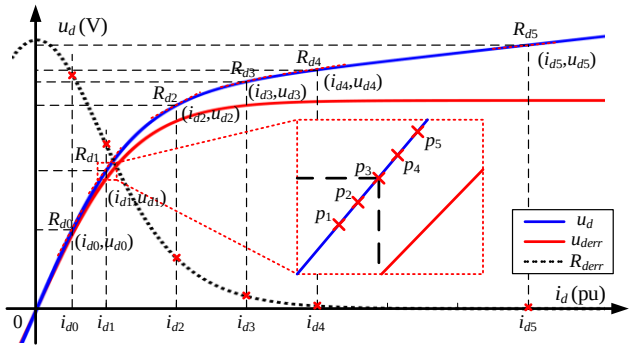

Fig. 8. *d*-axis voltage error characteristic of the inverter nonlinearities.

Considering the voltage as a function of the current, the voltage function $u_d(i_d)$ can be interpolated by Hermite polynomial to get the fitted mathematical expression under the premise of knowing several sets of data points of i_d, u_d and R_d. $u_d(i_d)$ is an odd function in the symmetrical curve about origin.

TABLE I
SAMPLING POINTS OF HERMITE INTERPOLATION

Sampling Point n	0	1	2	3	4	5
d-axis current i_d	i_{d0}	i_{d1}	i_{d2}	i_{d3}	i_{d4}	i_{d5}
d-axis voltage u_d	u_{d0}	u_{d1}	u_{d2}	u_{d3}	u_{d4}	u_{d5}
Resistance R_s	R_{d0}	R_{d1}	R_{d2}	R_{d3}	R_{d4}	R_{d5}

In order to fit the voltage error characteristics more effectively, the sampling points should cover all current regions especially the non-linear region at lower current level. Meanwhile, for improving the identification accuracy, more data points should be sampled for low current region with more obvious voltage error changes. Hence, 6 sets of data points are sampled corresponding to the current values of 0.05pu, 0.1pu, 0.2pu, 0.3pu, 0.4pu and 0.7pu. The sampled data points are corresponding to i_{d0} - i_{d5} shown in Fig. 8 and Table I, which will be used in the following calculations.

In order to minimize the data error, five points p_i, i=1, 2…5, near the data point are taken for the calculation of i_{dn}, u_{dn} and R_{dn}, as shown in Fig. 8. The solving equation of nth point are represented as

$$\begin{cases} i_{dn} = i_{dn-p3} \\ u_{dn} = \dfrac{1}{5}\displaystyle\sum_{i=1}^{5} u_{d-pi} \\ R_{dn} = \dfrac{5\displaystyle\sum_{i=1}^{5} i_{dn-pi}u_{dn-pi} - \left(\sum_{i=1}^{5} i_{dn-pi}\right)\left(\sum_{i=1}^{5} u_{dn-pi}\right)}{5\displaystyle\sum_{i=1}^{5} i_{dn-pji}^{\,2} - \left(\sum_{i=1}^{5} i_{dn-pi}\right)^2} \end{cases}. \tag{22}$$

As the influence of inverter nonlinearities can be neglected in high current level, the sampling value of resistance can be regarded as the stator resistance satisfying $R_{d5} \approx R_s$. The fitting function of the *d*-axis voltage in the interval of data points, expressed as (23), can be obtained through the Hermite interpolation whose derivation is given in Appendix.

$$U_{hermite}(i_d) = \sum_{n=0}^{5} h_n(i_d)u_d(i_{dn}) - \sum_{n=0}^{5} \overline{h_n}(i_d)R_d(i_{dn}),\ \zeta \in (i_{d0}, i_{d5})\,. \tag{23}$$

The *d*-axis error voltage can be approximately equivalent to be linear between 0 and the first data point and after the last data point. The voltage error u_{derr} can be given as

$$u_{derr}=\begin{cases}R_{d0}i_d-R_{d5}i_d, & 0\le i_d<i_{d0}\\ U_{hermite}(i_d)-R_{d5}i_d, & i_{d0}\le i_d<i_{d5}\\ u_{d5}-R_{d5}i_d, & i_{d5}\le i_d\end{cases}. \quad (24)$$

According to (24), the inverter nonlinearities of the *d*-axis can be compensated in the inductance identification. Furthermore, the inverter nonlinearities characteristics of each phase can be derived. In the resistance identification process, the injected signals are

$$\begin{cases}u_d=R_s i_d+\Delta u_{derr}(i_d)\\ u_q=0\\ i_d=i_d(t)\\ i_q=0\end{cases}. \quad (25)$$

Taking *a*-phase as an example, the phase voltage and current can be obtained by transforming (25) into the *abc* reference frame,

$$\begin{cases}u_a=u_d\cos(\theta_e)\\ i_a=i_d\cos(\theta_e)\end{cases}. \quad (26)$$

The error voltage of *abc*-phases can be represented as

$$u_{xerr}=u_{xerr}(i_x)=u_{derr}(i_x/\cos(\theta_e))\cos(\theta_e)\quad x=a,b,c. \quad (27)$$

The voltage error and resistance error of the *a*-phase and the *d*-axis at different current values and rotor positions are shown in Fig. 9, which is drawn by the inverter parameter equation in [26].

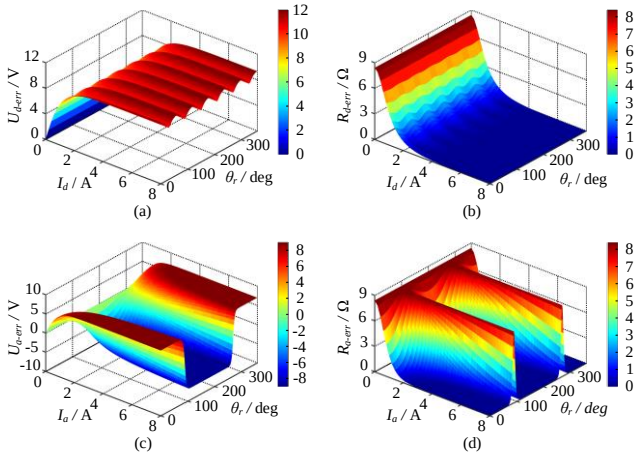

Fig. 9. Variation of voltage error and nonlinear equivalent resistance versus rotor position and current. (a) The voltage error in *d*-axis. (b) The nonlinear equivalent resistance in *d*-axis. (c) The voltage error in *a*-phase. (d) The nonlinear equivalent resistance in *a*-phase.

Fig. 9(a) and (b) show that, with the increase of i_d, u_{derr} increases gradually and R_{derr} decreases gradually. There is a 6th pulsation in an electrical cycle for u_{derr} and R_{derr}. Fig. 9(c) and (d) show that a 2nd pulsation exists in an electrical cycle for u_{aerr} and R_{aerr}.

The *abc*-phase currents are shown as

$$\begin{cases}i_a=i_d\cos(\theta_e)-i_q\sin(\theta_e)\\ i_b=i_d\cos(\theta_e-2\pi/3)-i_q\sin(\theta_e-2\pi/3)\\ i_c=i_d\cos(\theta_e+2\pi/3)-i_q\sin(\theta_e+2\pi/3)\end{cases}. \quad (28)$$

At the same time, the voltage error of the *q*-axis can be obtained by coordinate transformation,

$$\begin{aligned}u_{qerr}=&-\frac{2}{3}u_{aerr}(i_a)\sin(\theta_e)-\frac{2}{3}u_{berr}(i_b)\sin(\theta_e-\frac{2}{3}\pi)\\ &-\frac{2}{3}u_{cerr}(i_c)\sin(\theta_e+\frac{2}{3}\pi)\end{aligned}. \quad (29)$$

As in [26], the voltage error and the resistance error of the *q*-axis at different current values and rotor positions are shown in Fig. 10. There is a 6th pulsation in each electrical cycle.

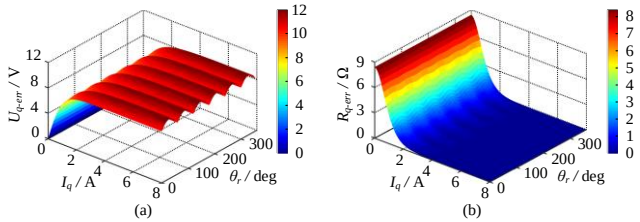

Fig. 10. Variation of voltage error and nonlinear equivalent resistance versus rotor position and current. (a) The voltage error in *q*-axis. (b) The nonlinear equivalent resistance in *q*-axis.

As shown in Fig. 9 and 10, R_{derr} and R_{qerr} trend to be 0 if the injected current is high enough, which properly explains why the resistance calculation should start from an enough high current point at a certain rotor position.

In summary, the inverter nonlinearity characteristics of *dq*-axes can be described by (24) and (29) and the compensation can be achieved by (21).

B. Error Analysis of Digital Time-Delay Effect and the Correction Method

In the digital control system of PMSM drives, there is an inevitable execution time delay, which is approximately 1.5 sampling periods [22]-[24]. This time delay is always neglected in fundamental frequency which is much lower than the frequency of the control signal. However, the frequency of the injected signal in inductance identification may be so high that the time delay can not be neglected. The influence of the digital time-delay effect on offline parameter self-learning has not been studied yet. The actual voltage injected into the *dq*-axes is behind the reference voltage in inductance identification. The time delay will lead to an additional flux linkage estimation error. In this part, the digital time-delay effect is discussed and a correction method is given.

Based on the physical characteristics of PMSMs, the *dq*-axis circuit can be equivalent to the RL circuit model. In the inductance identification process, square-wave voltage signals are injected into the *dq*-axes by ASI method. The actual and the reference values of voltage are expressed as follows,

$$\begin{aligned}u_{xact}(t)&=u_{xref}(t-T_s)\\ &=\begin{cases}U_{xout}, & nT_i+T_s\le t<(n+1)T_i+T_s\\ -U_{xout}, & (n+1)T_i+T_s\le t<(n+2)T_i+T_s\end{cases}\quad x=d,q\end{aligned} \quad (30)$$

where u_{xact} is the actual voltage taking time delay into account, T_i and T_s are the half sampling period and the delayed time, respectively. T_i can be represented as

$$T_i=-\tau\ln\left((U_{xout}-I_{xset}R_s)/(U_{xout}+I_{xset}R_s)\right). \quad (31)$$

$$i_x(t)=\begin{cases}-I_{xset}e^{-(t-nT_i-T_s)/\tau}+\dfrac{U_{xout}}{R_s}\left(1-e^{-(t-nT_i-T_s)/\tau}\right), & nT_i+T_s\le t<(n+1)T_i+T_s\\ I_{xset}e^{-(t-(n+1)T_i-T_s)/\tau}-\dfrac{U_{xout}}{R_s}\left(1-e^{-(t-(n+1)T_i-T_s)/\tau}\right), & (n+1)T_i+T_s\le t<(n+2)T_i+T_s\end{cases}\quad x=d,q \tag{32}$$

$$\psi_{xact}(t)=\begin{cases}-\tau\left(i_{xset}R_s+U_{xout}\right)e^{-(t-nT_i-T_s)/\tau}+\tau U_{xout}, & nT_i+T_s\le t<(n+1)T_i+T_s\\ \tau\left(i_{xset}R_s+U_{xout}\right)e^{-(t-(n+1)T_i-T_s)/\tau}-\tau U_{xout}, & (n+1)T_i+T_s\le t<(n+2)T_i+T_s\end{cases}\quad x=d,q \tag{33}$$

$$\psi_{xerr}(t)=\begin{cases}-\tau\left(I_{xset}R_s+U_{xout}\right)e^{-(t-nT_i-T_s)/\tau}+\tau U_{xout}, & nT_i+T_s\le t<(n+1)T_i\\ -\tau\left(I_{xset}R_s+U_{xout}\right)e^{-(t-nT_i-T_s)/\tau}+(\tau-t)U_{xout}, & (n+1)T_i\le t<(n+1)T_i+T_s\\ \tau\left(I_{xset}R_s+U_{xout}\right)e^{-(t-(n+1)T_i-T_s)/\tau}-(\tau+T_s)U_{xout}, & (n+1)T_i+T_s\le t<(n+2)T_i\\ \tau\left(I_{xset}R_s+U_{xout}\right)e^{-(t-(n+1)T_i-T_s)/\tau}-(\tau+T_s-t)U_{xout}, & (n+2)T_i\le t<(n+2)T_i+T_s\end{cases}\quad x=d,q \tag{34}$$

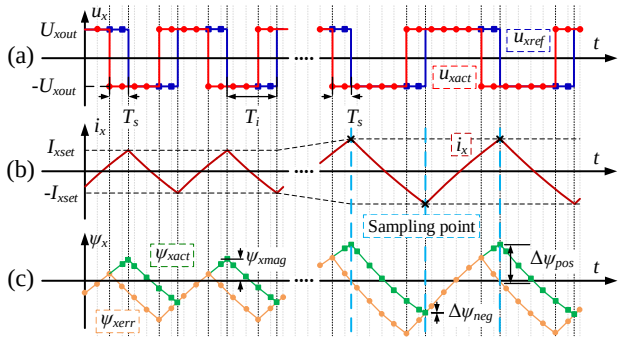

Fig. 11. Waveforms of digital signal process taking digital time delay into account. (a) Injected voltage reference and actual voltage with digital time delay. (b) Currents set in ASI control. (c) Flux linkage with time-delay error and flux linkage with digital time-delay compensation.

Based on the theory of RL circuit model, the *dq*-axis current can be transformed into (32), where R_s and L_x are the resistance and the inductance of the equivalent RL circuit respectively, and τ is the time constant of RL circuit satisfying $\tau=L_x/R_s$. i_x and u_{xref} can be directly acquired by control program. The actual and error waveforms of voltage, current and flux linkage can be described, as shown in Fig.11. $\Delta\psi_{pos}$ and $\Delta\psi_{neg}$ are the analytical estimation errors for the sampling points of positive current and negative current, respectively.

Substituting (30), (32) into (21), the actual flux linkage can be represented as (33). Considering the digital time delay effect, the flux linkage with time-delay error can be written as (34).

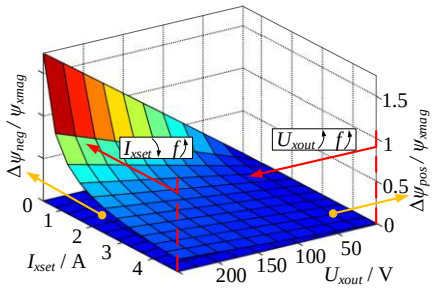

Fig. 12. Simulation results of digital time-delay error in the ASI method.

The curves of ψ_{xact} and ψ_{xerr} in Fig. 11(c) are in good agreement with the calculation results of (33) and (34). Fig. 11 shows that the flux linkage with time-delay error is theoretically less than the actual flux linkage. Considering the delay effect of the controller, the solving equation for the flux linkage can be expressed as

$$\psi_x=\int(u_{xref}(t-T_s)-u_{xerr}(i_x)-R_s i_x)\,\mathrm{d}t \quad x=d,q\,. \tag{35}$$

The errors caused by the digital time-delay effect is given in Fig. 12. As can be seen, ideally, $\Delta\psi_{neg}$ is a small value close to zero for any current setting I_{xset} and injected voltage U_{xout}. When the other parameters are fixed, the increase of U_{xout} and the decrease of I_{xset} will increase the frequency f of the injected signals in the ASI method, and further the errors become greater.

V. Experimental Results

The proposed self-commissioning method was validated on a 2.2-kW PMSM drive as shown in Fig. 13. The rated parameters of the PMSM are listed as follows: 380V, 5.6A, 50Hz, 21N·m and 1000r/min. The nameplate data are listed as follows: 2.75Ω for the stator resistance, 35mH for the *d*-axis inductance, 64mH for the *q*-axis inductance. The ARM STM32F103 is adopted to execute the whole parameter identification algorithm. The PWM switching frequency of the inverter is 6 kHz. An absolute encoder is applied to detect the initial position and the rotor rotation angle for parameter identification.

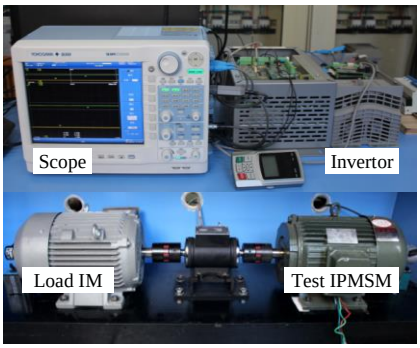

Fig. 13. Test platform of 2.2-kW PMSM drive.

The *a*-phase current of the whole identification process is shown in Fig. 14. It includes the initial position estimation, the stator resistance identification and the *dq*-axis flux linkage identification. The initial rotor position estimation adopts the scheme in [25] by HF signal injection. The rotor rotation angle

is also presented in Fig. 14. The flux linkage identification process would cause slight rotation of rotor. The electrical angle of rotor rotation is less than 8º. It can be considered that the motor is standstill in the process of parameter identification.

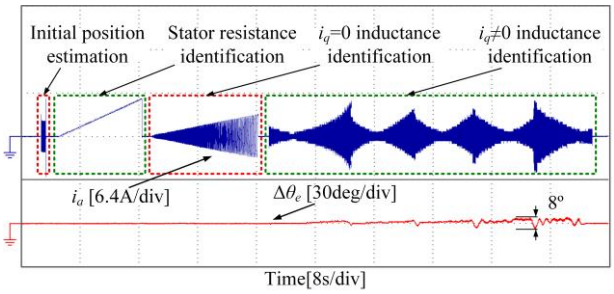

Fig. 14. *a*-phase current waveform of the whole offline identification.

Fig. 15 shows the experimental waveforms of the ASI method. U_{lim} and I_{lim} are set to be 300V and 7.5A, respectively. The *q*-axis current setting I_{qset} gradually increase, which is set to 3, 4, 5 and 6A. For a certain I_{qset}, i_d varies from 0 to the maximum value limited by I_{lim}. Therefore, the parameters can be identified for different combinations of i_d and i_q. For convenience and illustrative purposes, only four groups of I_{qset} are presented. In order to realize the parameter identification with more detail, more groups of I_{qset} can be measured. For a certain I_{qset}, the rotation angle increases with i_d. In general, the larger the I_{qset} is, the larger the motor angle will be. The electrical angle of rotor rotation is less than 8º for the whole inductance identification. The validity of the ASI method could be proved.

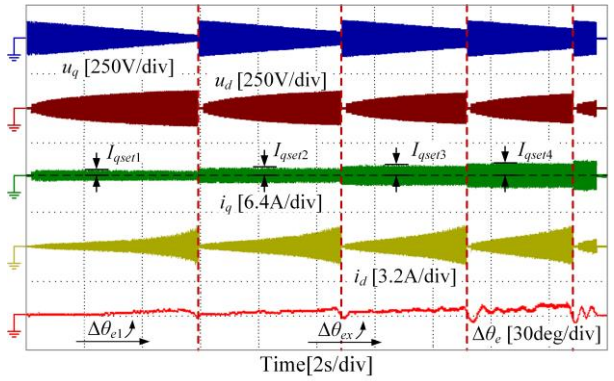

Fig. 15. Experimental waveforms of the hysteresis control with the proposed injection method in the inductance identification process.

The experimental results of the influence caused by inverter nonlinearities are shown in Fig. 16. Fig. 16(a) illustrates the experimental results of the current and voltage in the *d*-axis at θ_e=0. u_d is non-linear when the i_d is small. When i_d exceeds a certain value, u_d is linear with respect to i_d and the voltage error value u_{derr} is a large constant. At this time, the current-voltage slope is the stator resistance. The measured resistance values of several tests are between 2.71Ω and 2.81Ω which agree well with the motor nameplate value. u_{dfit} is the fitting value of u_d which is obtained by Hermite interpolation considering inverter nonlinearities by using (24). The fitting voltage is in good accordance with the test results. Fig. 16(b) and (c) show the voltage error characteristics of the inverter nonlinearities corresponding to the high frequency current of the *dq*-axes in inductance identification. The voltage errors in Fig. 16(b) and (c) present the value of u_{err} of equation (21), which can be directly compensated by (21) in real time during the inductance identification process. The voltage errors u_{derr} and u_{qerr} in the experimental waveform increase with the absolute value of the current, which is consistent with the theoretical analysis.

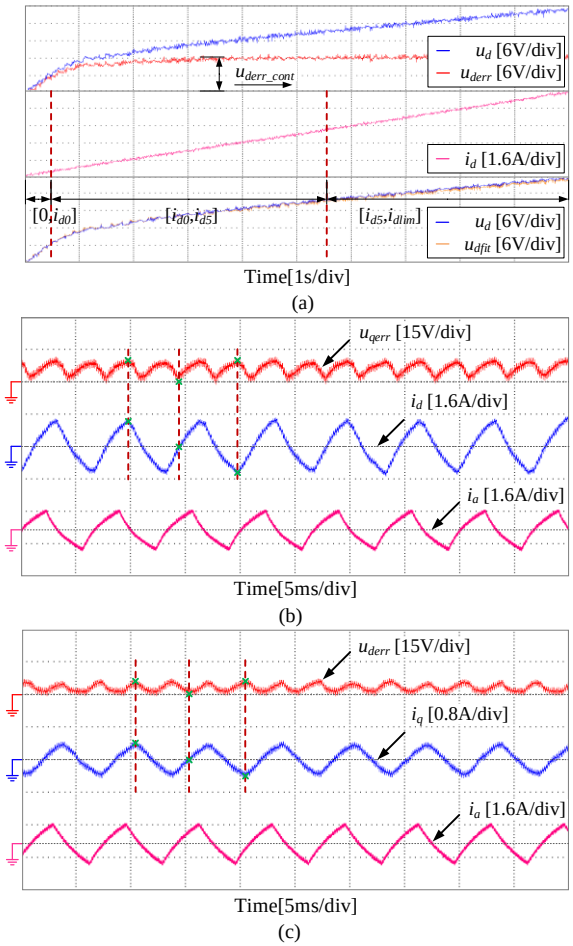

Fig. 16. Experimental results of the influence of inverter nonlinearities. (a) The voltage error of inverter nonlinearities in *d*-axis and the compensation voltage. (b) *d*-axis voltage error characteristics of the inverter nonlinearities. (c) *q*-axis voltage error characteristics of the inverter nonlinearities.

Fig. 17 shows the identified nonlinear equivalent resistance in the *d*-axis and the *a*-phase at different initial angles (0º-360º) with different injected *d*-axis currents. The injected *d*-axis currents are set to 1, 2, and 5 A respectively. Fig. 17(a) shows that R_{derr} decreases gradually with the increase of i_d. There are 6 pulsations in an electrical cycle for R_{derr}. The estimation error reaches the maximum at θ_e=(2*k*)*30º and the minimum at θ_e=(2*k*+1)*30º where *k*=0, 1⋯5. Fig. 17(b) describes the identification results of resistance error in *a*-phase with different injected *d*-axis currents based on (27). There are 2 pulsations in an electrical cycle for R_{aerr}. The maximum estimation error will be introduced at θ_e=90º and 270º, which keeps constant for different i_d. The minimum estimation error will be introduced at θ_e=0º and 180º, which decreases gradually with the increase of i_d. The experimental results show great agreement with the analytical results in Section IV.A.

This article has been accepted for publication in a future issue of this journal, but has not been fully edited. Content may change prior to final publication. Citation information: DOI 10.1109/TPEL.2019.2900559, IEEE Transactions on Power Electronics

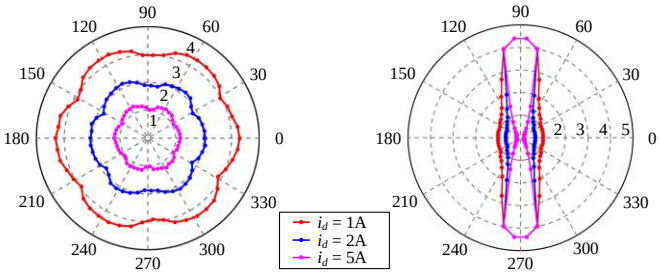

Fig. 17. Estimated results in an electrical cycle. (a) The equivalent resistance error in *d*-axis. (b) The equivalent resistance error in *a*-phase.

Fig.18 shows the waveforms of the current, voltage and flux linkage taking the digital time delay into account. The frequency of the experimental waveforms is 100 Hz. Because the actual value of voltage is delayed to the reference voltage, there is a fixed delay T_s between the voltage reference u_{dref}, flux error value ψ_{derr} and current value i_d, which is about 0.35 ms. The corrected voltage u_{dcor} eliminates the time delay between u_{dref} and i_d. At this time, the compensated flux linkage ψ_{dcor} is calculated, which has no time delay with i_d. Hence the u_{dcor} and ψ_{dcor} can be considered accurate. $\Delta\psi_{neg}$ is small enough to be neglected, and $\Delta\psi_{pos}$ is obvious with error of ψ_{dcor} being 16.3%. The experimental waveforms are in good agreement with the simulation results shown in Fig. 11 and Fig. 12. It can be concluded that the correction for digital time delay is necessary.

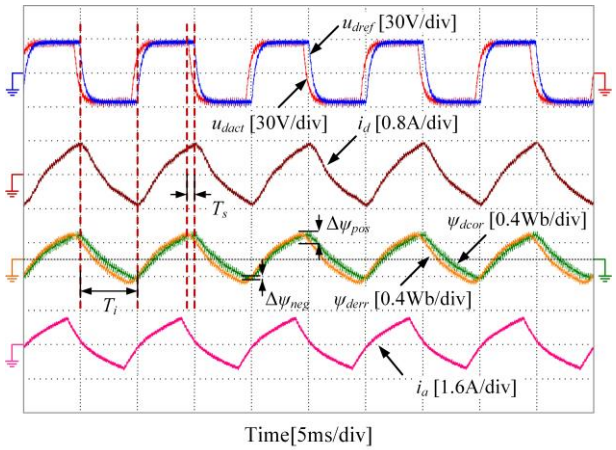

Fig. 18. Experimental waveforms with digital time delay in the inductance identification process.

The flux linkages of FEA obtained by the software FLUX and the flux linkages identified of the 2.2-kW test PMSM are shown in Fig. 19, along with the error. Fig. 19(a) shows that the identified *d*-axis flux linkage $\Delta\psi_d$ (Exp) is negative and the simulated *d*-axis flux linkage $\Delta\psi_d$ (FEA) is positive, between which the difference is 0.84Wb. The reason is that $\Delta\psi_d$ (Exp) is demagnetization flux linkage and $\Delta\psi_d$ (FEA) is total flux linkage including permanent magnet flux linkage ψ_f. According to (9), ψ_f is 0.84Wb. Fig. 19(b) is the error between $\Delta\psi_d$ (FEA) and $\Delta\psi_d$ (Exp) adding the permanent magnet flux linkage. The identified and simulated values of *q*-axis flux linkage in Fig. 19(c) can be directly compared. It can be concluded that *dq*-axes flux linkages are mostly affected by the current in the corresponding axis. The maximum error of *d*-axis flux is 3%, the maximum error of *q*-axis flux is 10%.

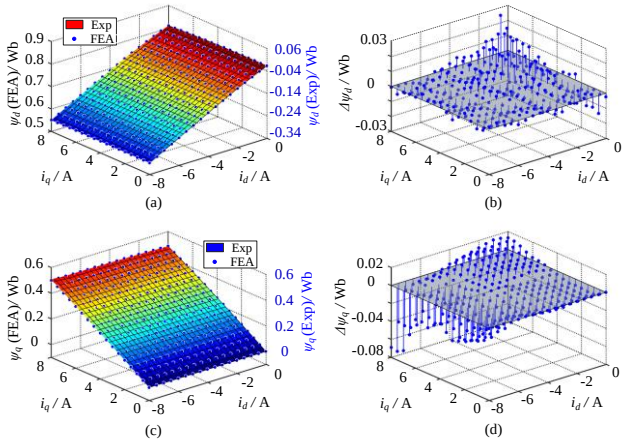

Fig. 19. Experimental and FEA results of flux linkage with respect to *dq*-axis currents. (a) Experimental and FEA results of ψ_d. (b) Error between experimental and FEA results of ψ_d. (c) Experimental and FEA results of ψ_q. (d) Error between experimental and FEA results of ψ_q.

Fig.20 shows the inductances of FEA and the inductances identified of the 2.2-kW test PMSM, along with the error, from which it can be seen the good fitting accuracy. Through Fig. 20(a) and (g), it is found that L_{dd} and L_{qq} increase when i_d decreases, and L_{dd} and L_{qq} decrease when i_q increases due to the magnetic saturation. The maximum variation percentage of L_{dd} is 22.2%, and the maximum variation percentage of L_{qq} is 17.1%. The mutual inductances of *dq*-axes L_{dq} and L_{qd} are approximately equal. When i_q is 0, there is no armature reaction of *q*-axis, so L_{dq} and L_{qd} are 0. On the contrary, when i_q increases or i_d decreases, the degree of armature reaction of *q*-axis increases along with the mutual inductances. The error is within the acceptable level. When i_d = -8A and i_q = 0, the inductances are unsaturated whose values are 36.1mH and 63.7mH for L_{dd} and L_{qq}, which is close to the nameplate value. The mutual inductances reach 15% of *d*-axis inductance and 7.7% of *q*-axis inductance at their peak values which are too large to be neglected.

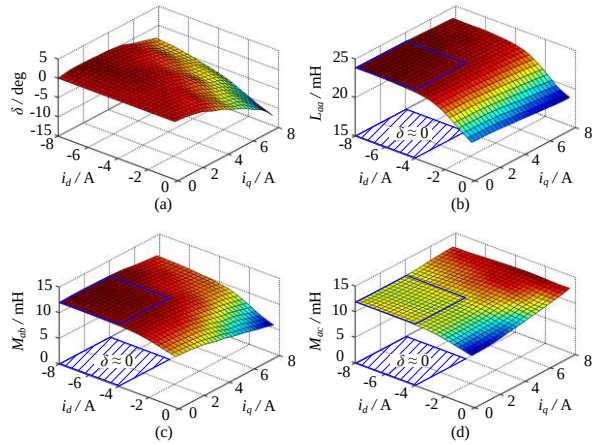

Fig. 21. Experimental and FEA results of inductance with respect to *dq*-axis currents. (a) Experimental results of angle of cross-coupling δ, (b) Experimental results of L_{aa}, (c) Experimental results of M_{ab}, (d) Experimental results of M_{ac}.

Fig.21 shows the bias angle δ of *q*-axis armature reactance, the self-inductance of *a*-phase L_{aa}, the mutual inductance between *a*-phase and *b*-phase M_{ab} and the mutual inductance between *a*-phase and *c*-phase M_{ac} when θ_e = 0. The magnitude

This article has been accepted for publication in a future issue of this journal, but has not been fully edited. Content may change prior to final publication. Citation information: DOI 10.1109/TPEL.2019.2900559, IEEE Transactions on Power Electronics

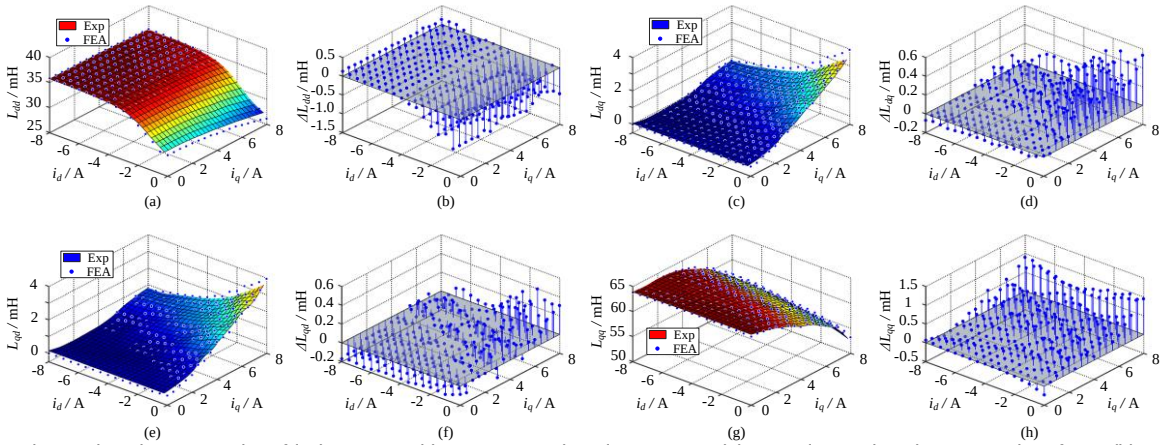

Fig. 20. Experimental and FEA results of inductance with respect to *dq*-axis currents. (a) Experimental and FEA results of L_{dd}. (b) Error between experimental and FEA results of L_{dd}. (c) Experimental and FEA results of L_{dq}. (d) Error between experimental and FEA results of L_{dq}. (e) Experimental and FEA results of L_{qq}. (f) Error between experimental and FEA results of L_{qq}. (g) Experimental and FEA results of L_{qd}. (h) Error between experimental and FEA results of L_{qd}.

of M_{ab} and M_{ac} are positively associated with the absolute value of the bias angle δ of *q*-axis armature reactance. L_{aa} has the same trend as self-inductance of *d*-axis L_{dd}. In traditional control methods, the mutual inductance between *dq*-axes and armature reaction are neglected, which means δ is 0 and M_{ab} is equal to M_{ac} when θ_e is 0. However, the experimental results show that δ is close to 0 only when the i_q is small and the demagnetization current is large (the absolute value of $-i_d$ is large), and M_{ab} is equal to M_{ac} only in the dashed area, as shown in Fig21 (b), (c) and (d).

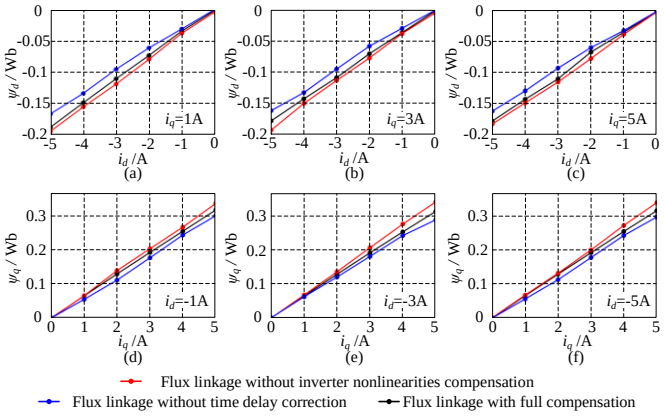

Fig. 22. Estimated *dq* axis flux linkage in an electrical cycle with and without error compensation. (a) Estimated ψ_d before and after error compensation at i_q=1A. (b) Estimated ψ_d before and after error compensation at i_q=3A. (c) Estimated ψ_d before and after error compensation at i_q=5A. (d) Estimated ψ_q before and after error compensation at i_d=-1A. (e) Estimated ψ_q before and after error compensation at i_d=-3A. (f) Estimated ψ_q before and after error compensation at i_d=-5A.

The identified flux linkages with and without error compensation at different current level are compared, as shown in Fig. 22. The flux linkage in *d*-axis with inverters nonlinearities compensation is smaller than that without compensations, and the flux linkages in *q*-axis are opposite. The reason is that the absolute value of the voltage term in (21) decreases after the inverter nonlinearities compensation, which makes the absolute value of the identified flux linkage in *dq*-axes smaller. At the same time, the error of inverters nonlinearities of flux linkages in *dq*-axes increases with the absolute values of i_d and i_q, because the integral of (21) increases the error with the current. The flux linkage in *d*-axis without digital time delay correction is slightly smaller than that without correction, and the flux linkage in *q*-axis without time delay correction is obviously greater than that without correction. The theoretical analysis in Section IV.B proves the accuracy of the experimental results.

VI. Conclusion

This paper investigates the offline parameter self-learning method considering inverter nonlinearities and the digital time-delay effect. The hysteresis control based ASI method achieved the flux linkage identification for different combinations of i_d and i_q at standstill. The voltage error characteristic caused by inverter nonlinearities was identified by Hermite interpolation function in the stator resistance identification and was compensated during inductance estimation. The digital time-delay effect was analyzed and corrected in the signal injection process. The proposed ASI method achieved the flux linkage identification for different combinations of id and i_q. The spatial flux linkage maps of *dq*-axes and the spatial inductance maps of *dq*-axes were obtained along with the stator resistance. The experimental results demonstrate the influence of the magnetic saturation and the cross-coupling on inductances and prove the existence of the mutual inductance between *dq*-axes. Furthermore, the *abc*-phase inductances were calculated by the proposed algorithm. The estimated flux linkages and inductances were validated via FEA and the experimental results confirm the practicability of the ASI method for general-purpose drive applications. The identified parameters considering the cross-coupling and mutual inductance can be directly applied into various machine control scheme, and its application prospect will be studied in the future research.

VII. Appendix

For a function $f(x)$, the function can be interpolated with k+1 data points x_0, x_1, x_2,…, x_k, and values $f(x_0)$, $f(x_1)$,…, $f(x_k)$ and $f'(x_0), f'(x_1),\ldots, f'(x_k)$. Thus, Hermite interpolation of $f(x)$ can be expressed as,

$$H(x)=\sum_{n=0}^{k}h_n(x)f(x_n)-\sum_{n=0}^{k}\overline{h_n}(x)f'(x_n) \tag{A1}$$

where

$$\begin{cases} h_n(x)=\left[1-2(x-x_n)l_n'(x_n)\right]l_n^{\,2}(x) & n=0,1,\cdots,k \\ \overline{h_n}(x)=(x-x_n)l_n^{\,2}(x) & n=0,1,\cdots,k \\ l_n(x)=\dfrac{p_{k+1}(I)}{(x-x_n)p_{k+1}'(I_x)} & n=0,1,\cdots,k \\ p_{k+1}(x)=(x-x_0)\cdots(x-x_k) \end{cases} \tag{A2}$$

The error function of Hermite interpolation can be given by

$$E(x)=\frac{p_{k+1}(x)^2}{(2k+2)!}f^{2k+2}(\zeta)\qquad \zeta\in(x_0,x_k). \tag{A3}$$

REFERENCES

[1] K. Liu, J. Feng, S. Guo, L. Xiao and Z. Zhu, "Identification of Flux Linkage Map of Permanent Magnet Synchronous Machines Under Uncertain Circuit Resistance and Inverter Nonlinearity," IEEE Trans. Ind. Informat., vol. 14, no. 2, pp. 556-568, Feb. 2018.

[2] Z. Liu, H. Wei, X. Li, K. Liu and Q. Zhong, "Global Identification of Electrical and Mechanical Parameters in PMSM Drive Based on Dynamic Self-Learning PSO," IEEE Trans. Power Electron., vol. 33, no. 12, pp. 10858-10871, Dec. 2018.

[3] P. L. Xu and Z. Q. Zhu, "Carrier Signal Injection-Based Sensorless Control for Permanent-Magnet Synchronous Machine Drives Considering Machine Parameter Asymmetry," IEEE Trans. Ind. Electron., vol. 63, no. 5, pp. 2813-2824, May 2016.

[4] H. Ge, Y. Miao, B. Bilgin, B. Nahid-Mobarakeh and A. Emadi, "Speed Range Extended Maximum Torque Per Ampere Control for PM Drives Considering Inverter and Motor Nonlinearities," IEEE Trans. Power Electron., vol. 32, no. 9, pp. 7151-7159, Sept. 2017.

[5] G. Feng, C. Lai, J. Tjong and N. C. Kar, "Noninvasive Kalman Filter Based Permanent Magnet Temperature Estimation for Permanent Magnet Synchronous Machines," IEEE Trans. Power Electron., vol. 33, no. 12, pp. 10673-10682, Dec. 2018.

[6] G. Pellegrino, B. Boazzo and T. M. Jahns, "Magnetic Model Self-Identification for PM Synchronous Machine Drives," IEEE Trans. Ind. Appl., vol. 51, no. 3, pp. 2246-2254, May. 2015.

[7] A. Pouramin, R. Dutta, M. F. Rahman and D. Xiao, "Inductances of a fractional-slot concentrated-winding interior PM synchronous machine considering effects of saturation and cross magnetization," in Proc. IEEE Energy Convers. Congr. Expo. (ECCE), 2015, pp. 6075–6081.

[8] S. A. Odhano, P. Pescetto, H. A. A. Awan, M. Hinkkanen, G. Pellegrino and R. Bojoi, "Parameter Identification and Self-Commissioning in AC Motor Drives: a Technology Status Review," IEEE Trans. Power Electron., to be published. doi: 10.1109/TPEL.2018.2856589.

[9] S. Wiedemann, S. Hall, R. M. Kennel and M. Alaküla, "Dynamic Testing Characterization of a Synchronous Reluctance Machine," IEEE Trans. Ind. Appl., vol. 54, no. 2, pp. 1370-1378, March. 2018.

[10] S. A. Odhano, R. Bojoi, Ş. G. Roşu and A. Tenconi, "Identification of the Magnetic Model of Permanent-Magnet Synchronous Machines Using DC-Biased Low-Frequency AC Signal Injection," IEEE Trans. Ind. Appl., vol. 51, no. 4, pp. 3208-3215, July. 2015.

[11] P. Pescetto and G. Pellegrino, "Automatic Tuning for Sensorless Commissioning of Synchronous Reluctance Machines Augmented With High-Frequency Voltage Injection," IEEE Trans. Ind. Appl., vol. 54, no. 5, pp. 4485-4493, Sept. 2018.

[12] G. Wang, L. Qu, H. Zhan, J. Xu, L. Ding, G. Zhang, D. Xu, "Self-Commissioning of Permanent Magnet Synchronous Machine Drives at Standstill Considering Inverter Nonlinearities," IEEE Trans. Power Electron., vol. 29, no. 12, pp. 6615-6627, Dec. 2014.

[13] L. Peretti, P. Sandulescu and G. Zanuso, "Self-commissioning of flux linkage curves of synchronous reluctance machines in quasi-standstill condition," IET Elect. Power Appl., vol. 9, no. 9, pp. 642-651, Nov. 2015.

[14] M. Hinkkanen, P. Pescetto, E. Mölsä, S. E. Saarakkala, G. Pellegrino and R. Bojoi, "Sensorless Self-Commissioning of Synchronous Reluctance Motors at Standstill Without Rotor Locking," IEEE Trans. Ind. Appl., vol. 53, no. 3, pp. 2120-2129, May. 2017.

[15] N. Bedetti, S. Calligaro and R. Petrella, "Stand-Still Self-Identification of Flux Characteristics for Synchronous Reluctance Machines Using Novel Saturation Approximating Function and Multiple Linear Regression," IEEE Trans. Ind. Appl., vol. 52, no. 4, pp. 3083-3092, July. 2016.

[16] Y. Qi, M. Zafarani, B. Akin and S. E. Fedigan, "Analysis and Detection of Inter-Turn Short-Circuit Fault Through Extended Self-Commissioning," IEEE Trans. Ind. Appl., vol. 53, no. 3, pp. 2730-2739, May. 2017.

[17] C. Wu, C. Guo, Z. Xie, F. Ni and H. Liu, "A Signal-Based Fault Detection and Tolerance Control Method of Current Sensor for PMSM Drive," IEEE Trans. Ind. Electron., vol. 65, no. 12, pp. 9646-9657, Dec. 2018.

[18] Y. Qi and B. Akin, "Severity Estimation of Inter Turn Short Circuit Fault for PMSM," IEEE Trans. Ind. Electron., to be published. doi: 10.1109/TIE.2018.2879281.

[19] Z. Tang and B. Akin, "Suppression of Dead-Time Distortion Through Revised Repetitive Controller in PMSM Drives," IEEE Trans. Energy Convers., vol. 32, no. 3, pp. 918-930, Sept. 2017.

[20] S. M. Seyyedzadeh and A. Shoulaie, "Accurate Modeling of the Nonlinear Characteristic of a Voltage Source Inverter for Better Performance in Near Zero Currents," IEEE Trans. Ind. Electron., vol. 66, no. 1, pp. 71-78, Jan. 2019.

[21] L. M. Gong and Z. Q. Zhu, "A Novel Method for Compensating Inverter Nonlinearity Effects in Carrier Signal Injection-Based Sensorless Control From Positive-Sequence Carrier Current Distortion," IEEE Trans. Ind. Appl., vol. 47, no. 3, pp. 1283-1292, May. 2011.

[22] G. Wang, L. Yang, B. Yuan, B. Wang, G. Zhang and D. Xu, "Pseudo-Random High-Frequency Square-Wave Voltage Injection Based Sensorless Control of IPMSM Drives for Audible Noise Reduction," IEEE Trans. Ind. Electron., vol. 63, no. 12, pp. 7423-7433, Dec. 2016.

[23] Bon-Ho Bae and Seung-Ki Sul, "A compensation method for time delay of full-digital synchronous frame current regulator of PWM AC drives," IEEE Trans. Ind. Appl., vol. 39, no. 3, pp. 802-810, May. 2003.

[24] J. Yim, S. Sul, B. Bae, N. R. Patel and S. Hiti, "Modified Current Control Schemes for High-Performance Permanent-Magnet AC Drives With Low Sampling to Operating Frequency Ratio," IEEE Trans. Ind. Appl., vol. 45, no. 2, pp. 763-771, March. 2009.

[25] X. Jin, R. Ni, W. Chen, F. Blaabjerg and D. Xu, "High-Frequency Voltage-Injection Methods and Observer Design for Initial Position Detection of Permanent Magnet Synchronous Machines," IEEE Trans. Power Electron., vol. 33, no. 9, pp. 7971-7979, Sept. 2018.

[26] Y. Park and S. K. Sul, "A novel method utilizing trapezoidal voltage to compensate for inverter nonlinearity", IEEE Trans. Power Electron., vol. 27, no. 12, pp. 4837-4846, Dec. 2012.

Qiwei Wang received the B.S. and M.S. degrees in electrical engineering from the Harbin Institute of Technology, Harbin, China, in 2005 and 2007, respectively, where he is currently working toward the Ph.D. degree in power electronics and electrical drives in the School of Electrical Engineering and Automation.

His current research interests include parameter identification technique, and PMSM position sensorless control.

Guoqiang Zhang (M'18) received the B.S. degree in Electrical Engineering from Harbin Engineering University, Harbin, China, in 2011, and the M.S. and Ph.D. degrees in Electrical Engineering from Harbin Institute of Technology, Harbin, China, in 2013 and 2017, respectively.

Since then, he has been a Postdoctoral Fellow and a Lecturer in the Department of Electrical Engineering, Harbin Institute of Technology. His current research interests include parameter identification technique, and control of electrical drives, with main focus on sensorless field-oriented control of interior permanent magnet synchronous machines.

Dr. Zhang serves as an Associate Editor for *Journal of Power Electronics*.

Gaolin Wang (M'13) received the B.S., M.S., and Ph.D. degrees in electrical engineering from the Harbin Institute of Technology, Harbin, China, in 2002, 2004, and 2008, respectively.

In 2009, he as a Lecturer joined the Department of Electrical Engineering, Harbin Institute of Technology, where he has been a Full Professor of electrical engineering since 2014. From 2009 to 2012, he was a Postdoctoral Fellow with Shanghai Step Electric Corporation, where he was involved in the traction machine control for direct-drive elevators. He has authored more than 60 technical papers published in journals and conference proceedings. He is the holder of ten Chinese patents. His current major research interests include permanent magnet synchronous motor drives, high-performance direct-drive for traction systems, position sensorless control of ac motors, efficiency optimization control of PMSM, and digital control of power converters.

Dr. Wang serves as an Associate Editor for *IET Electric Power Applications* and *Journal of Power Electronics*. He was the recipient of the Outstanding Research Award and the Delta Young Scholar Award from the Delta Environmental and Educational Foundation in 2012 and 2014, respectively. He is currently supported by the National Natural Science of China for Excellent Young Scholars, the Program for Basic Research Excellent Talents, and the Young Talent Program from the Harbin Institute of Technology.

Chengrui Li (S'16) received the B.S. degree in Electrical Engineering from Harbin Institute of Technology, Harbin, China, in 2015, where he is currently working toward the Ph.D. degree in power electronics and electrical drives in the School of Electrical Engineering and Automation.

His current research interests include parameter identification technique, and control of electrical drives, with main focus on sensorless field-oriented control of synchronous reluctance machines and synchronous reluctance machine design.

Dianguo Xu (M'97–SM'12–F'17) received the B.S. degree in control engineering from the Harbin Engineering University, Harbin, China, in 1982, and the M.S. and Ph.D. degrees in electrical engineering from the Harbin Institute of Technology (HIT), Harbin, China, in 1984 and 1989, respectively.

In 1984, he joined the Department of Electrical Engineering, HIT, as an Assistant Professor. Since 1994, he has been a Professor with the Department of Electrical Engineering, HIT. He was the Dean of the School of Electrical Engineering and Automation, HIT, from 2000 to 2010, and was the Assistant President of the HIT from 2010 to 2014. He is currently the Vice President of the HIT. He authored or co-authored more than 600 technical papers. His research interests include renewable energy generation technology, power quality mitigation, sensorless vector controlled motor drives, high-performance PMSM servo system.

Dr. Xu is an Associate Editor for the IEEE TRANSACTIONS ON INDUSTRIAL ELECTRONICS and the IEEE JOURNAL OF EMERGING AND SELECTED TOPICS IN POWER ELECTRONICS. He serves as the Chairman of the IEEE Harbin Section.